Numerical Simulation of Carbon Sputtering for Electric Propulsion in the Ground Facility

IEPC-2022-379

Presented at the 37th International Electric Propulsion Conference
Massachusetts Institute of Technology, Cambridge, MA, USA
June 19-23, 2022

Keita Nishii[1], Sean Clark[2], Joshua Tompkins[3], Nakul Nuwal[4], Deborah A. Levin[5], and Joshua L. Rovey[6]
University of Illinois at Urbana-Champaign, Urbana-Champaign, Illinois, 61801, USA.

Backsputtering causes carbon contamination in an electric propulsion (EP) facility, which is a well-known concern in EP testing. The need to isolate facility contamination effects from on-orbit performance and wear characteristics grows as EP systems evolve toward larger power levels (~100 kW). Both physics-based modeling and fundamental experiments are required to achieve high-fidelity tracking of sputtered carbon in a ground facility. This study focused on the numerical tracking of the sputtered carbon in the ground facility using PIC/DSMC method. We have extended our in-house multi-GPU PIC/DSMC solver to the ground testing environment and demonstrated thruster plume simulation and carbon sputtering inside. Two types of the sputtering model were also compared by changing incident angle of the ion beam. This study was the first use of the incident angle-dependent sputtering model in a DSMC calculation.

I. Introduction

High-power electric propulsion (EP) is a critical component of manned-spaceflight design beyond low-Earth orbit. NASA, for example, has proved that a 40 kW-class solar electric propulsion capability may be established for both near-term and long-term designs and science missions [1]. However, the necessity to correctly simulate the space environment and the operating lifetimes, which often reach tens of thousands of hours, creates problems for developing and validating high-power systems [2, 3]. Backsputtering is one of the biggest concerns for higher-power EP testing [4]. Backsputtering rates increases when the bombardment energy is increased. Although test facilities are lined with graphite to reduce the impact, investigations have demonstrated that the deposition on the thruster still occurs [5]. Front pole coverings made of graphite were also adopted to prevent the possibility of the magnetic circuit being degraded [6]. Despite the erosion-resistant material, backsputtered facility carbon still deposits on thruster surfaces, resulting in high uncertainties in the measurement of both thruster component erosion rates and the proportion of deposited carbon films associated with thruster erosion [7].

Numerical modeling can differentiate and monitor all sputtered carbon particles in the ground facility. Understanding where particles travel in the test chamber is aided by particle simulation. Carbon backsputtering has been studied quantitatively in various papers [3, 8]. Gilland et al. [3] have used the Direct Simulation Monte Carlo (DSMC) approach to calculate the sputter rate and carbon deposition rate in the ground facility, as well as to simulate all vacuum chamber domains and solve carbon flux in the vacuum chamber. Choi et al. [8] calculated the fluxes of backsputtered carbon arriving on the boron nitride inner and outer discharge channel surfaces, as well as the origins of the carbon. However, specific information on the sputtering yield of a particular graphitic structure as a function of incoming ion type, ion energy, ion angle, temperature, and surface morphology should be necessary for these Particle-In-Cell (PIC) models [9, 10].

[1]Postdoctoral Researcher, Department of Aerospace Engineering, University of Illinois, Urbana-Champaign.
[2]Ph.D. student, Department of Aerospace Engineering, University of Illinois, Urbana-Champaign.
[3]Ph.D. student, Department of Aerospace Engineering, University of Illinois, Urbana-Champaign.
[4]Ph.D. student, Department of Aerospace Engineering, University of Illinois, Urbana-Champaign.
[5]Professor, Department of Aerospace Engineering, University of Illinois, Urbana-Champaign.
[6]Associate Professor, Department of Aerospace Engineering, University of Illinois, Urbana-Champaign.

The accuracy of the sputter modeling is one of the challenging aspects, especially for the low-energy ion bombardment to non-metallic material such as carbon. Although, many studies have proposed semi-analytical theories to estimate sputter yields for ion-elemental targets [11–16], these analytical formulations tend to underestimate experimental sputter yield at the low ion energy values (100–1000 eV) expected in EP environments. Moreover, these semi-empirical models cannot adequately capture the sputtering rates in covalently-bonded structures such as graphite, which undergo amorphization during ion bombardment. The reported sputtering rates for pyrolytic graphite are also found to be inconsistent among experimental studies in the literature, which has been speculated to be due to the contributions of surface roughness [15, 17].

Both physics-based modeling and fundamental experiments are required to overcome the limits of current ground testing capabilities. One of the objectives of Joint Advanced Propulsion Institute (JANUS), which is exploring high-power electric propulsion systems for human exploration by NASA, is to understand how the backsputtered carbon particle is transported from facility walls and graphite front pole covers of the thruster. Successful completion of the proposed studies in JANUS will establish physics-based limits, mitigation techniques, and extrapolation procedures to provide a probabilistic assessment of the in-space performance and lifetime of high-power ($\sim$ 100 kW) EP devices. Through this project, we will clarify the backsputtered carbon transportation through the following three complementary and integrated activities: (1) predicting sputter yield of graphite under low energy xenon bombardment by molecular dynamics (MD) simulations, (2) tracking sputtered carbon through the relevant facility and thruster plume environments using the PIC/DSMC method, and (3) developing a new carbon isotope tracking diagnostic to directly measure carbon transport in ground-based facilities.

This paper reports the work related to numerical carbon tracking (approach No. 2). The first objective of this study is to implement modules for simulating ground facilities in our in-house code. The particle boundary conditions are important to achieve a high background pressure compared to the space in which the propulsion system is actually operated. The second objective is to simulate carbon sputtering with approaches that reproduce more accurate sputtered carbon distribution. Using information from the calculated thruster plume, we have simulated the carbon sputtered from the target placed downstream of the thruster. We used an angle-dependent distribution function based on the results of previous studies [18], in addition to the conventionally used simplest model, the cosine distribution.

II. Method

A. PIC/DSMC modeling

PIC is a well-known kinetic method for calculating the time-evolving properties of charged particles in plasma and their interactions with the induced electric field. In addition, the well-known particle-based DSMC technique is required to represent the collisions. However, when computing the full vacuum chamber, the number of particles and cells rises, increasing the computational cost. Jambunathan and Levin [19] demonstrated the accuracy and scalability of the in-house 3-D multi-GPU PIC/DSMC solver called the Cuda-based Hybrid Approach for Octree Simulations (CHAOS). The CHAOS code has been used extensively for the in-space environment [20–22] and is expanding to the ground facility environment as an initial work of numerical tracking of sputtered carbon particles in this study.

We simulated the thruster operation in the ground facility at the University of Illinois at Urbana-Champaign. The schematic of the numerical geometry is shown in Fig. 1. The thruster exit is located at (x, y, z) = (0.3, 0.6, 0.6 m), and its diameter is 0.1 m. In our numerical simulation, the calculation domain was enclosed by diffuse walls. When the particles hit the wall, the particle energy was accommodated with the wall temperature of 300 K, and they were neutralized if they were ions. The cylinder domain size was 1.2 m in diameter and 2.4 m in length. The chamber background density was controlled by numerical pumps, which removed any particle reaching inside them [23]. The numerical pump was installed downstream, as shown in Fig. 1-(b). This geometry was based on the actual position where the cryopump (CVI Corp., TORRMASTER TM-1200) was installed.

The calculation conditions of this study were based on a previous study [23]. We use a quasi-neutral approach and a Boltzmann electron temperature model described in Ref. [21]. Three types of collisions are considered: momentum exchange (MEX) among neutral collisions [24], MEX among neutral and ions pairs [25], and charge–exchange collisions between ions and neutrals [26]. Gaseous xenon is introduced into the computational domain at the thruster exit at each time step. Table 1 presents the exit conditions used in this work. The injected neutral particles are taken from a half-Maxwellian distribution with a temperature of 250 K. In contrast, a mono-energetic function equivalent to a 40,000 m/s exit x-velocity with a divergence angle of 15 deg is used for the ejected ions. The simulations are run for 300,000-time steps and were sampled for 200,000-time steps. The real particle to simulated particle ratio was

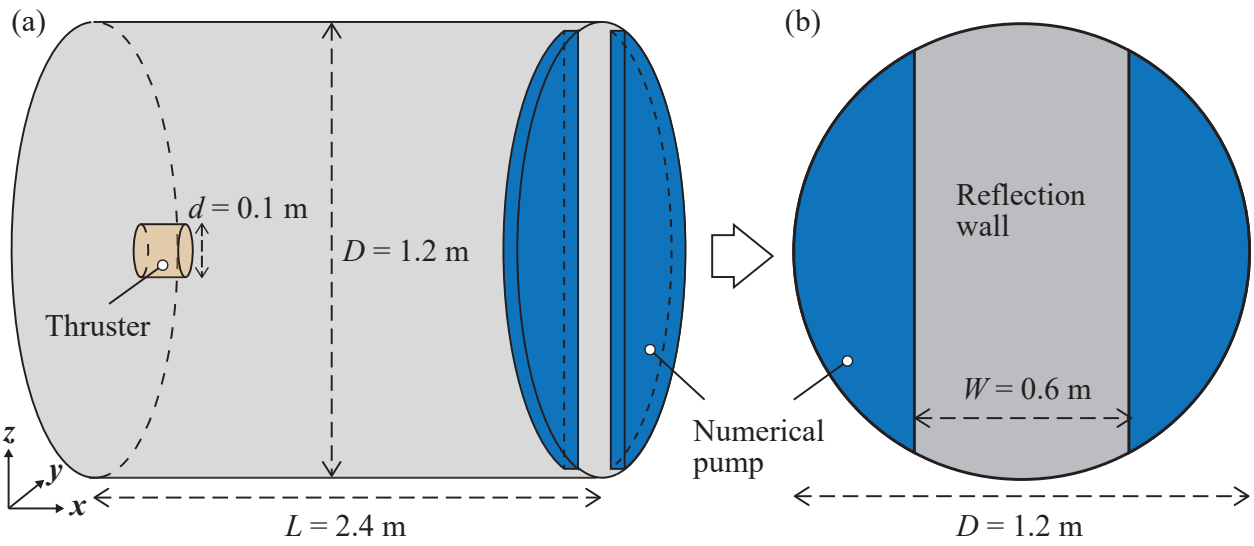

Fig. 1 Schematics of the calculation geometry and the numerical pumps. Figure (a) shows the cylinder geometry of the vacuum chamber. Figure (b) shows the numerical pump viewed from the axial direction. The blue area is the numerical pump, which deletes computational particles when they enter the area.

$F_{\mathrm{num}} = 5.5 \times 10^9$ for both neutral and ion particles.

Table 1 Thruster exit flow conditions and calculation parameters for each particle.

Particle	Number density (m^{-3})	Bulk velocity (m/s)	Time step (s)	Weighting factor
Xe neutral	4.6×10^{17}	200	4.88×10^{-6}	1.0
Xe ion	2.3×10^{15}	40,000	2.44×10^{-8}	0.005

B. Carbon Sputter Modeling

Figure 2 (a) shows the planned experiment that will be carried out at the University of Illinois at Urbana-Champaign. The target, the carbon monolith, will be placed downstream, and the sputter yield will be measured. This study aimed to simulate this configuration for the demonstration of carbon transport modeling. Figure 2 (b) shows the numerical geometry in this study near the carbon target. The carbon target, which had 1 cm in diameter, was placed 10 cm downstream from the thruster exit. We identified the incident ion flux, angle, and energy from the PIC/DSMC simulation described in the previous section. Then, we simulated sputtered carbon from the target by DSMC, assuming no interaction between xenon thruster plume and sputtered carbon (over-lay method). The sputtered carbon flux was measured where the thruster exit plane was located, as seen in Fig. 2 (b).

The following part of this section describes how the carbon particle was introduced in the DSMC method. First, this study only simulates atomic carbon neutrals (C) for simplicity, although Oyarzabal et al. [15] have shown carbon clusters (e.g. C^2 and C^3) might have a significant impact on the sputtering simulation. The following methods also assumed all sputtered particles were mono-atomic carbon. We also assumed the sticking coefficient of the carbon particle was unity, which means the computational carbon particles were deleted from the calculation when they hit any walls.

Total sputter yield was calculated according to Yim's paper [27]. He surveyed low energy (< 1000 eV) xenon ion impact sputter yield to provide a more coherent baseline set of sputter yield data and accompanying fits for electric propulsion integration. He showed the parameters of Eckstein's equation [13, 28] and Wei's equation [29] for xenon-graphite sputtering. When calculating total sputter yield, $Y(E, \theta)$, the energy dependence is typically calculated for yields at normal incidence, $Y_0(E)$, and then the angular dependence, $Y^{'}(\theta)$, is then subsequently applied as a multiplicative factor as follows:

$$Y(E, \theta) = Y_0(E) \cdot Y^{'}(\theta). \tag{1}$$

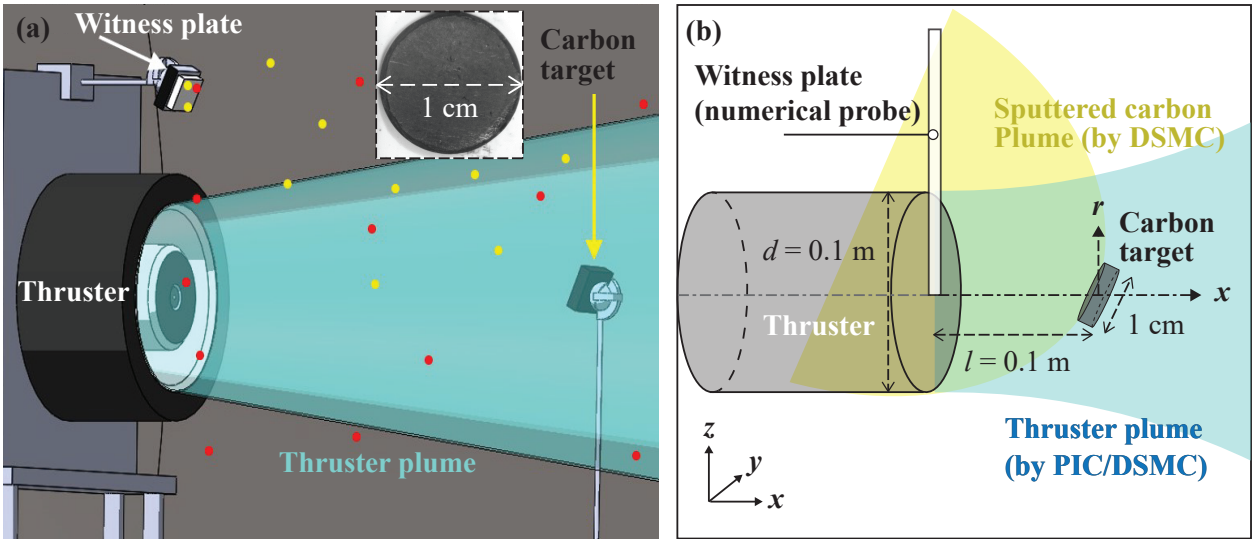

Fig. 2 The schematic of the test for carbon sputtering. Figure (a) indicates experimental geometries to be carried out in the future. Figure (b) shows numerical geometries in this study.

Sputter yields at normal incidence, $Y_0(E)$, can be calculated by the following equation [13, 28]:

$$Y_0(E) = Q s_n \frac{\left(\frac{E}{E_{\text{th}}} - 1\right)^{\mu}}{\frac{\lambda}{w} + \left(\frac{E}{E_{\text{th}}} - 1\right)^{\mu}}, \tag{2}$$

$$s_{\text{n}} = \frac{0.5 \ln\left(1 + 1.2288\epsilon\right)}{w}, \tag{3}$$

$$w = \epsilon + 0.1728\sqrt{\epsilon} + 0.008\epsilon^{0.1504}, \tag{4}$$

$$\tag{5}$$

where Q, μ, and λ are free parameters, E_{th} is the threshold energy, s_{n} is reduced nuclear stopping power based on the krypton–carbon potential, and ϵ is reduced energy. Yim [27] obtained $Q = 4.0$, $\mu = 1.8$, $\lambda = 1.8$, and $E_{\text{th}} = 21$ eV as a result of the Markov chain Monte Carlo fitting by using experimental data of xenon-carbon sputtering. Reduced energy, ϵ, is a function of incident ion energy and can be calculated as follows:

$$\epsilon = \frac{a_{\text{L}}}{Z_i Z_s} \frac{4\pi\varepsilon}{e^2} \frac{M_s}{M_i + M_s} E, \tag{6}$$

$$a_{\text{L}} = \left(\frac{9\pi^2}{128}\right)^{1/3} a_0 \left(Z_i^{2/3} + Z_s^{2/3}\right)^{-1/2}, \tag{7}$$

where a_{L} is Lindhard screening length, a_0 is Bohr radius, Z is atomic number, ε is vacuum permittivity, e is elementary charge, M is atomic mass, and subscriptions i and s mean projectile ion species and target surface material, respectively. The angular dependence, $Y^{'}(\theta)$, can be calculated as the following equation [29]:

$$Y^{'}(\theta) = \frac{1}{\sqrt{1 + (\beta/\alpha)^2 \tan^2\theta}} \exp\left(\frac{1}{2}\left(\frac{a}{\alpha}\right)^2 \left[1 - \frac{1}{\sqrt{1 + (\beta/\alpha)^2 \tan^2\theta}}\right]\right). \tag{8}$$

where a, α, and β are free parameters. Similarly to $Y(E, \theta)$, Yim's study [27] showed that the maximum likelihood values were $\beta/\alpha = 0.88$ and $a/\alpha = 2.05$, respectively.

The energy, E, of sputtered particles from a surface is characterized using the Sigmund-Thompson energy distribution [14, 16]. The energy distribution function, $f(E)$, can be described as follows:

$$f(E) \propto \frac{E}{(E + E_{\text{B}})^{3-2m}}, \tag{9}$$

where $E_B = 7.4$ eV is the binding energy, and $m = 1/3$ is the interatomic potential exponent parameter [8]. This study assumed that the particle energy follows this energy distribution function, with the maximum value being the energy of the colliding ions. This function takes maximum value when $E = E_B/2(1-m)$. We reproduced this probability function in our DSMC code using rejection sampling, a Monte Carlo technique.

This study considered two types of angular distribution: cosine distribution and experimental fitting distribution obtained by Williams et al. [18]. Cosine distributions are commonly assumed in most wear models of electric propulsion devices [3, 8]. On the other hand, Williams et al. [18] measured polar-angle-dependent differential sputter yields, y(θ), and fit the measured data to a cosine polynomial as follows:

$$y(\theta) = \begin{cases} \sum_{n=1}^{5} A_n \cos^n \theta, & \text{if } \theta \geq 0, \\ \sum_{n=1}^{5} B_n \cos^n \theta, & \text{if } \theta < 0, \end{cases} \tag{10}$$

where A_i, and B_i are the fitting coefficients dependent on the ion incident energy and incident angle for front sputtering ($\theta \geq 0$) and back sputtering ($\theta < 0$), respectively. Figure 3 shows the cosine distribution and differential sputter yield data measured in Ref [18]. The actual sputtering behavior can be dramatically different than ideal behavior assumed in models where cosine distributions are used. When assuming Williams' differential sputter yield fitting, the distribution function in polar angle, $f(\theta)$, can be described as follows:

$$f(\theta) \propto \sin\theta \cdot y(\theta). \tag{11}$$

We reproduced this probability function by using rejection sampling and assumed uniform distribution in the azimuthal direction, ϕ ($0 < \phi < \pi$).

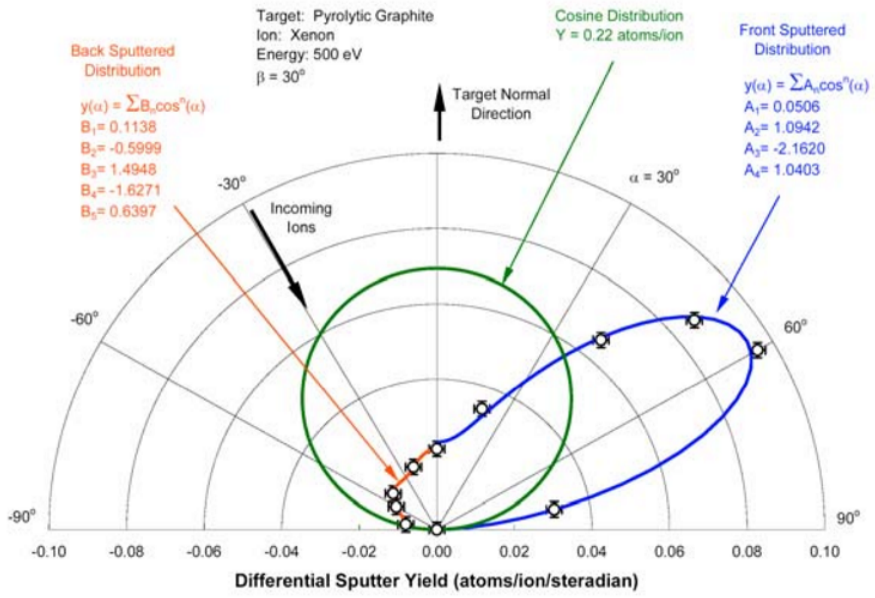

Fig. 3 Cosine distribution and differential sputter yield data measured in Ref [18] when the incidence angle was 30° and ion energy was 500 eV.

III. Result and Discussion

A. Thruster Plume in the Ground Facility

At a steady state, the total number of the computational particle was 2.7×10^7 (2.5×10^7 for neutrals and 1.9×10^6 for ions). Because the ions were neutralized once they reflected off the wall, most of the computational particles inside the domain were neutrals. The average background density was 3.68×10^{16} m^{-3}, which was equivalent to 1.15×10^{-6}

torr at 300 K. The pumping speed of the numerical pump was 32.3 kL/s. According to the reference,[30] the actual test environment was at the pressures of 2.5×10^{-6} – 2.5×10^{-5} torr. Therefore, the simulated condition were reasonable for EP testing.

Figure 4 shows the calculation result on the center plane of the calculation domain (y = 0.6 m plane). As seen in Figs. (a) and (b) the neutral and ion had the highest density near the thruster exit. The CEX population also had a peak near the thruster exit, but they were observed to expand into the backflow region due to the potential gradient, as seen in Fig. (d).

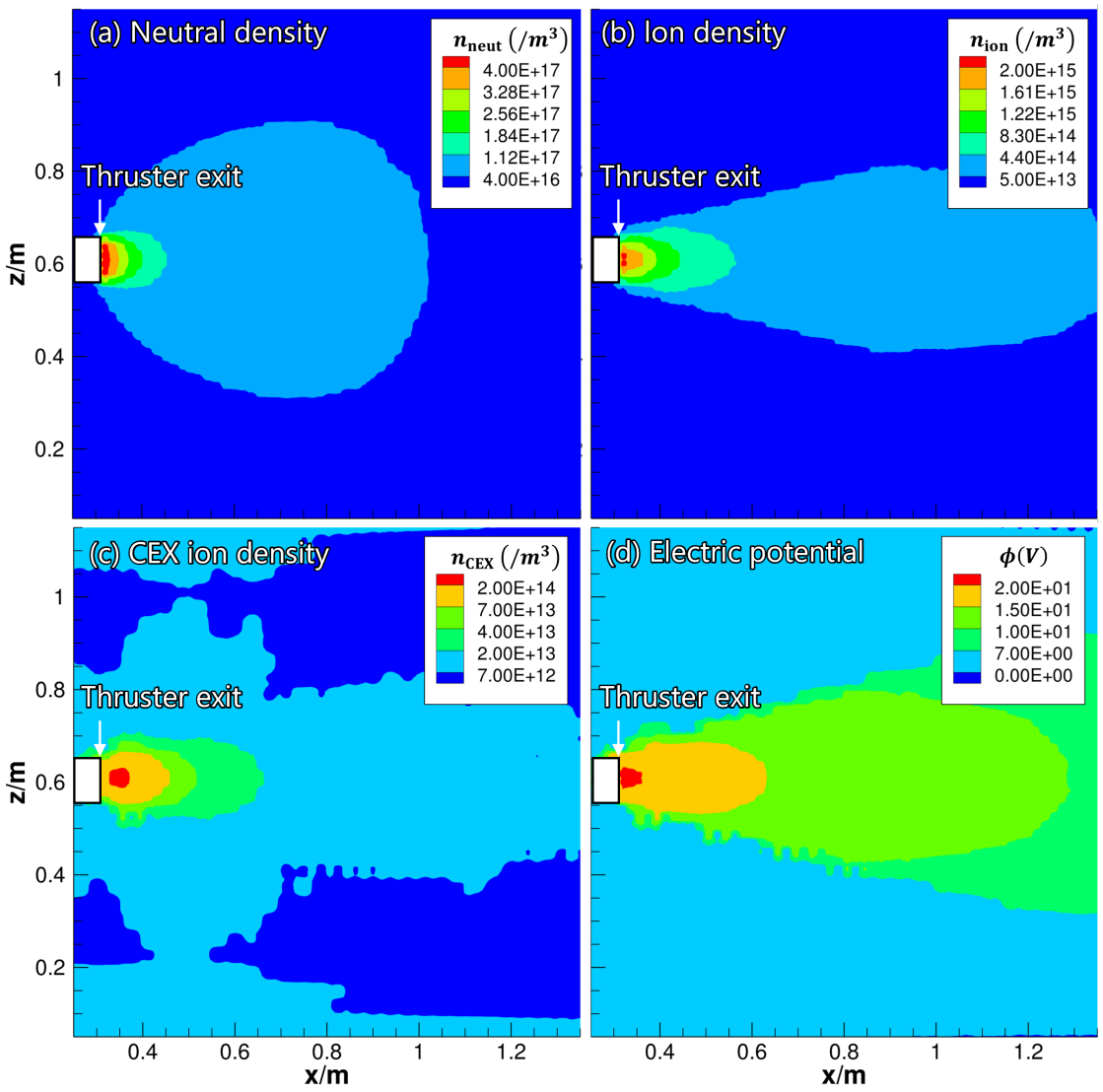

Fig. 4 Calculation results of 2-D field values on the center plane of the calculation domain (y = 0.6 m plane); (a) neutral density, (b) ion density, (c) CEX ion density, and (d) electric potential.

To clarify the effect of CEX ions on sputtering, we directly sampled computational CEX ions every 5 steps from 450,000 to 500,000-time steps. Five locations were selected for the sampling, as shown in Fig. 5. The lower plots in Fig. 5 show the histogram of the sampled computational CEX ions. The ion energies in the plume core region, such as locations 1 and 2, were smaller than that in the backflow region, such as locations 4 and 5. According to Yim's study [27], the threshold energy of the xenon-carbon sputtering was 21 eV. Therefore, the CEX ion can be negligible when considering the sputtering in this study because the carbon sputtering target was placed in the plume core region (location 1).

To determine the conditions of the sputtered carbon, we also sampled beam ions that went through the carbon target

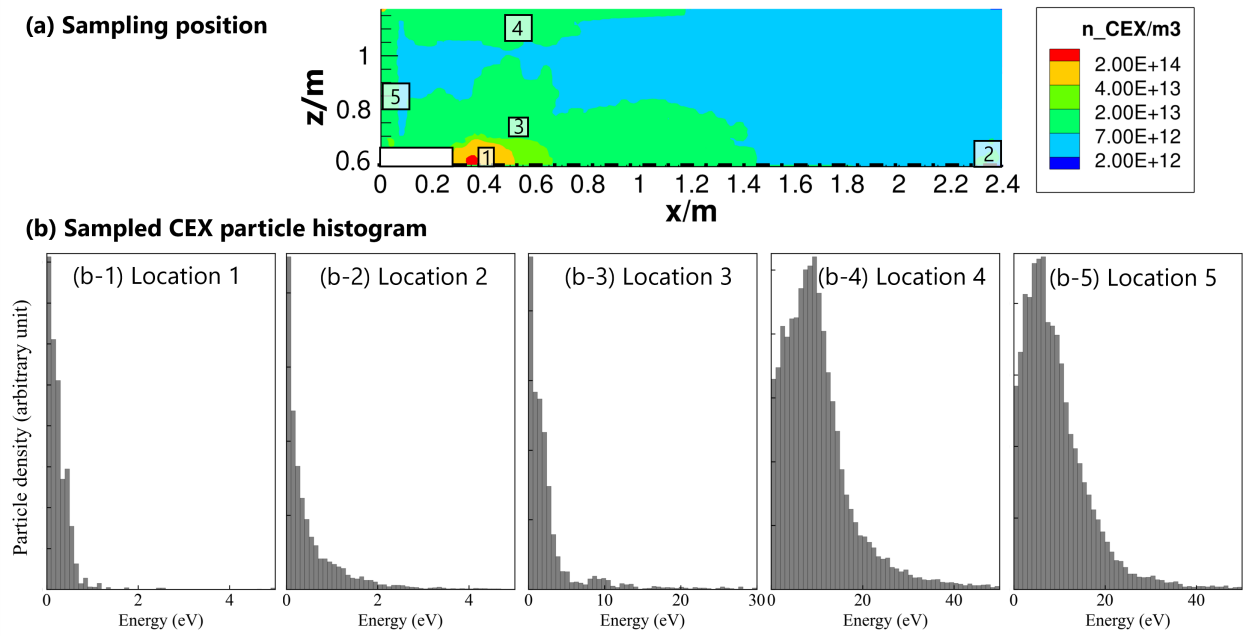

Fig. 5 The result of the direct sampling of computational CEX ions. The upper figure shows the locations of the sampling. The lower plots show the histograms of the CEX ion energy at each sampling location.

location, as shown in Fig. 2 (b). Figure 6 shows the histograms of the sampled ions without CEX ions. The leftmost plot shows the probability of the incident position in r, which is the distance from the central axis of the target. The linear distribution in the r direction means the uniform flux, and the measured flux was 3.85×10^{19} ion/(m^{2}s). The incident angle, shown in the center plot, also showed linear distribution, but the maximum angle was 1.0 degrees, which was sufficiently small enough to be approximated as zero. The rightmost plot shows that the ion energy was constant at around 1000 eV, almost the same as the inflow condition, and that the width of the distribution was small (cold plasma). In summary, we can assume uniform ion flux of 3.85×10^{19} ion/(m^{2}s), x-direction incident angle, and the constant incident energy of 1000 eV from the ion sampling result.

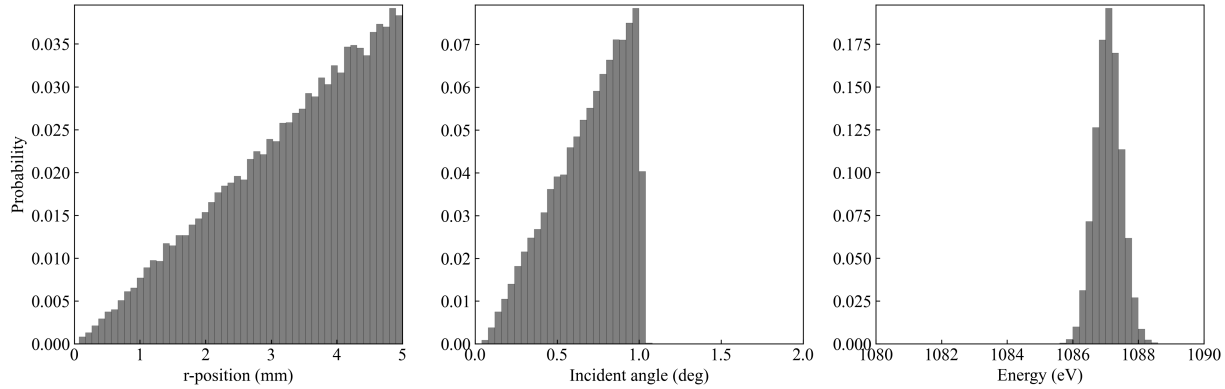

Fig. 6 The histograms of the sampled computational particle at the carbon target position (Fig. 2). The computational particles were 53,367 in total as a result of sampling between 400,000 and 500,000 steps. The r in the leftmost plot is the distance from the central axis of the target as shown in Fig. 2 (b).

B. Transportation of the Sputtered Carbon

Based on the method described in Section II.B, mono-atomic carbons were introduced from the position where the carbon target was placed. The sputter yield was 0.360 and 1.047 for 0 degrees and 45 degrees, respectively. Figure 7 shows the number density of the carbon sputtered from the carbon target by changing the incident angle and angular distribution model of the sputtered carbon at the center (y=0.6 m) plane. There were differences between the cosine distribution and Williams's distribution. Especially when the incident angle was 45 degrees, compared to Figures 7 (b) and (d), Williams's density distribution (d) became narrower along the z-direction.

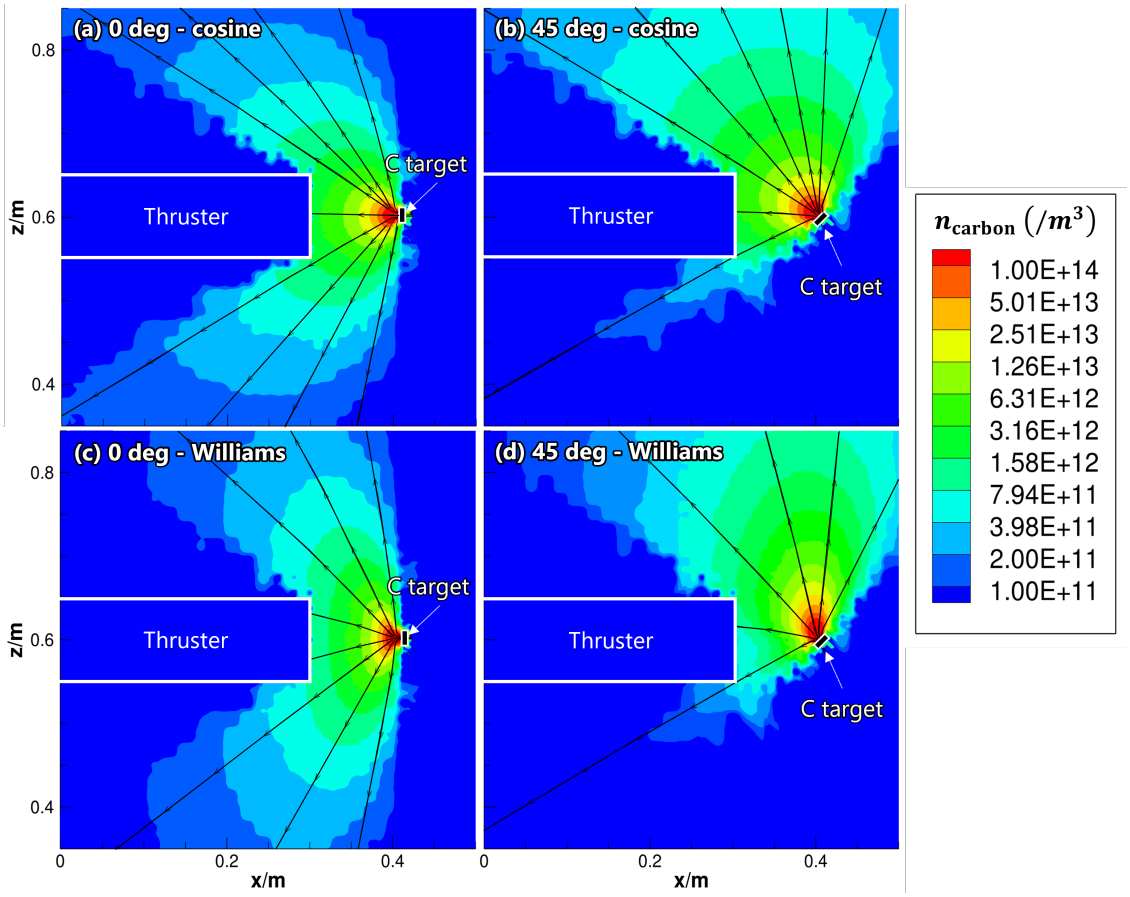

Fig. 7 The number density of the carbon sputtered from the carbon target (C target) by changing the incident angle and angular distribution model of the sputtered carbon at the center (y=0.6 m) plane. Figures (a) and (b) are the result when the cosine distribution is assumed. Figures (c) and (d) are the result when Williams's distribution [18]. is assumed. The black arrows show the streamlines of the sputtered carbon in those planes.

For quantitative investigation of the sensitivity of carbon flux to the sputtering model, we sampled carbon particles across witness plate as shown in Fig. 2 (b). Figure 8 shows the carbon flux in z-direction for 0 degrees and 45 degrees, respectively. When using Williams's model, the maximum flux was less than half of the cosine distribution, but in areas far from the thruster center axis, the flux exceeded that of the cosine distribution. When the target angle was 45 degrees (Fig. 8-b), the peak position moved from the center to a larger position in the z-direction. There were two peaks in the case of Williams's model, which was reflected in the measured sputtering yield due to the complex mechanism of carbon sputtering as described in the Introduction section.

IV. Conclusion

This study has extended the in-house 3-D multi-GPU PIC/DSMC solver, CHAOS, and demonstrated thruster plume simulation and carbon sputtering in the ground facility. The particle wall boundaries and numerical pump worked

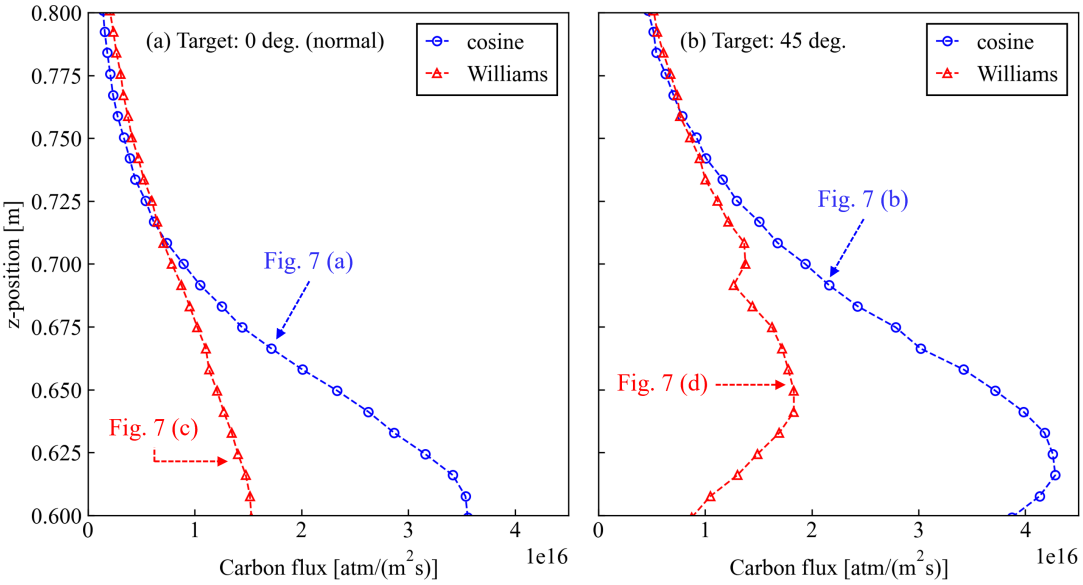

Fig. 8 Carbon flux sampled at $x = 0.3$ m and $y = 0.6$ m line (thruster front position n Fig. 7). Figure (a) shows the flux when the carbon target was placed at 0 degrees, and (normal direction) as shown in Figs. 7 (a) and (c). Figure (b) shows the flux when the carbon target was placed at 45 degrees as shown in Figs. 7 (b) and (d).

successfully. Our calculations included the carbon sputtering for the entire vacuum chamber simulation, depending on the energy and angle of the incident particles. This is a the first use of this method for solving sputtered carbon transportation.

We consider three model updates for accuracy: electrical potential modeling, geometry modeling, and sputtering modeling. First, our current result assumed quasi-neutrality and Boltzmann relation for the electric potential calculation. We will carry out kinetic modeling because sheath effects may significantly impact collision energy, especially in regions with a large amount of CEX ions. Second, an accurate geometry model, especially pump modeling, is also crucial for high-fidelity calculations. Third, as our results show, the sputtering model significantly impacts the distribution of carbon in the chamber. However, it is difficult to adequately model the movement of carbon after sputtering in current research. Further modeling of sputtered particles is desirable through the JANUS project.

Acknowledgments

This work was partially supported by NASA through the Joint Advanced Propulsion Institute, a NASA Space Technology Research Institute, grant number 80NSSC21K1118. This work used the Extreme Science and Engineering Discovery Environment (XSEDE) Expanse at the San Diego Supercomputer Center through allocation TG-PHY220010, which is supported by the National Science Foundation.

References

[1] Herman, D. A., Santiago, W., Kamhawi, H., Polk, J. E., Snyder, J. S., Hofer, R. R., and Sekerak, M. J., "The Ion Propulsion System for the Asteroid Redirect Robotic Mission," *52nd AIAA/SAE/ASEE Joint Propulsion Conference*, AIAA Propulsion and Energy Forum, American Institute of Aeronautics and Astronautics, 2016.

[2] Elliott, F., Foster, J., and Patterson, M., "An Overview of the High Power Electric Propulsion (HiPEP) Project," *40th AIAA/ASME/SAE/ASEE Joint Propulsion Conference and Exhibit*, Joint Propulsion Conferences, American Institute of Aeronautics and Astronautics, 2004.

[3] Gilland, J. H., Williams, G., Burt, J. M., and Yim, J., "Carbon Back Sputter Modeling for Hall Thruster Testing," *52nd AIAA/SAE/ASEE Joint Propulsion Conference*, AIAA Propulsion and Energy Forum, American Institute of Aeronautics and Astronautics, 2016.

[4] Polk, J. E., "The Effect of Carbon Deposition on Accelerator Grid Wear Rates in Ion Engine Ground Testing," *36th AIAA/ASME/SAE/ASEE Joint Propulsion Conference and Exhibit*, American Institute of Aeronautics and Astronautics, 2000.

[5] Williams, G., Haag, T., Foster, J., Van Noord, J., Malone, S., Hickman, T., and Patterson, M., "Analysis of the Pyrolytic Graphite Ion Optics Following the 2000-hour Wear Test of the HiPEP Ion Thruster," *42nd AIAA/ASME/SAE/ASEE Joint Propulsion Conference & Exhibit*, Joint Propulsion Conferences, American Institute of Aeronautics and Astronautics, 2006.

[6] M. Sekerak, R. Hofer, J. Polk, B. Jorns, I. Mikellides, "Wear Testing of a Magnetically Shielded Hall Thruster at 2000 s Specific Impulse," *Joint Conference of 30 th International Symposium on Space Technology and Science, 34 th International Electric Propulsion Conference and 6 th Nano-satellite Symposium*, 2017.

[7] Williams, G. J., Jr, Gilland, J. H., Peterson, P. Y., Kamhawi, H., Huang, W., Ahern, D. M., Yim, J., Herman, D. A., Hofer, R. R., and Sekerak, M., "Wear testing of the HERMeS thruster," *AIAA/SAE/ASEE Joint Propulsion Conference*, American Institute of Aeronautics and Astronautics, 2016.

[8] Choi, M., Yim, J. T., Williams, G. J., Herman, D. A., and Gilland, J. H., "Hybrid-PIC Simulation of Backsputtered Carbon Transport in the Near-Field Plume of a Hall Thruster," *35th International Electric Propulsion Conference*, 2017, pp. 1–13.

[9] Kim, S.-P., and Lee, K.-R., "Molecular Dynamics Study of Ballistic Rearrangement of Surface Atoms during High Energy Ion Bombardment on Pd (001) Surface," *Technical Proceedings of the 2008 NSTI Nanotechnology Conference and Trade Show*, Vol. 1, 2008.

[10] Kim, S.-P., Chew, H. B., Chason, E., Shenoy, V. B., and Kim, K.-S., "Nanoscale mechanisms of surface stress and morphology evolution in FCC metals under noble-gas ion bombardments," *Proceedings of the Royal Society A: Mathematical, Physical and Engineering Sciences*, Vol. 468, No. 2145, 2012, pp. 2550–2573.

[11] Yamamura, Y., and Shindo, S., "An empirical formula for angular dependence of sputtering yields," *Radiat. Eff.*, Vol. 80, No. 1-2, 1984, pp. 57–72.

[12] Yamamura, Y., and Tawara, H., "ENERGY DEPENDENCE OF ION-INDUCED SPUTTERING YIELDS FROM MONATOMIC SOLIDS AT NORMAL INCIDENCE," *At. Data Nucl. Data Tables*, Vol. 62, No. 2, 1996, pp. 149–253.

[13] Eckstein, W., and Preuss, R., "New fit formulae for the sputtering yield," *J. Nucl. Mater.*, Vol. 320, No. 3, 2003, pp. 209–213.

[14] Sigmund, P., "Sputtering by ion bombardment theoretical concepts," *Sputtering by Particle Bombardment I: Physical Sputtering of Single-Element Solids*, edited by R. Behrisch, Springer Berlin Heidelberg, Berlin, Heidelberg, 1981, pp. 9–71.

[15] Oyarzabal, E., Doerner, R. P., Shimada, M., and Tynan, G. R., "Carbon atom and cluster sputtering under low-energy noble gas plasma bombardment," *J. Appl. Phys.*, Vol. 104, No. 4, 2008, p. 043305.

[16] Gnaser, H., "Energy and Angular Distributionsof Sputtered Species," *Sputtering by Particle Bombardment: Experiments and Computer Calculations from Threshold to MeV Energies*, Springer Berlin Heidelberg, Berlin, Heidelberg, 2007, pp. 231–328.

[17] Tartz, M., Neumann, H., Leiter, H., and Esch, J., "Pyrolytic graphite and carbon-carbon sputter behaviour under xenon ion incidence," *29th International Electric Propulsion Conference*, 2005.

[18] Williams, J., Johnson, M., and Williams, D., "Differential Sputtering Behavior of Pyrolytic Graphite and Carbon-Carbon Composite Under Xenon Bombardment," *40th AIAA/ASME/SAE/ASEE Joint Propulsion Conference and Exhibit*, Joint Propulsion Conferences, American Institute of Aeronautics and Astronautics, 2004.

[19] Jambunathan, R., and Levin, D. A., "CHAOS: An octree-based PIC-DSMC code for modeling of electron kinetic properties in a plasma plume using MPI-CUDA parallelization," *J. Comput. Phys.*, Vol. 373, 2018, pp. 571–604.

[20] Nuwal, N., and Levin, D., "Correction: Kinetic modeling of parasitic currents on spacecraft surfaces due to ambient space plasmas," *AIAA Propulsion and Energy 2019 Forum*, American Institute of Aeronautics and Astronautics, Reston, Virginia, 2019, pp. 1–11.

[21] Nuwal, N., Jambunathan, R., and Levin, D. A., "Kinetic Modeling of Spacecraft Surfaces in a Plume Backflow Region," *IEEE Trans. Plasma Sci. IEEE Nucl. Plasma Sci. Soc.*, Vol. 48, No. 12, 2020, pp. 4305–4325.

[22] Nuwal, N., and Levin, D. A., "Influence of secondary electron emission on plasma-surface interactions in the low earth orbit environment," *Plasma Sources Sci. Technol.*, Vol. 30, No. 3, 2021, p. 035015.

[23] Korkut, B., Levin, D. A., and Tumuklu, O., "Simulations of Ion Thruster Plumes in Ground Facilities Using Adaptive Mesh Refinement," *J. Propul. Power*, Vol. 33, No. 3, 2017, pp. 681–696.

[24] Oh, D., and Hastings, D., "Experimental verification of a PIC-DSMC model for Hall thruster plumes," *32nd Joint Propulsion Conference and Exhibit*, Joint Propulsion Conferences, American Institute of Aeronautics and Astronautics, 1996.

[25] Araki, S. J., and Wirz, R. E., "Ion–Neutral Collision Modeling Using Classical Scattering With Spin-Orbit Free Interaction Potential," *IEEE Trans. Plasma Sci. IEEE Nucl. Plasma Sci. Soc.*, Vol. 41, No. 3, 2013, pp. 470–480.

[26] Miller, J. S., Pullins, S. H., Levandier, D. J., Chiu, Y. H., and Dressler, R. A., "Xenon charge exchange cross sections for electrostatic thruster models," *J. Appl. Phys.*, Vol. 91, No. 3, 2002, pp. 984–991.

[27] Yim, J. T., "A survey of xenon ion sputter yield data and fits relevant to electric propulsion spacecraft integration," *The 35th International Electric Propulsion Conference*, 2017.

[28] Eckstein, W., "Sputtering Yields," *Sputtering by Particle Bombardment: Experiments and Computer Calculations from Threshold to MeV Energies*, Springer Berlin Heidelberg, Berlin, Heidelberg, 2007, pp. 33–187.

[29] Wei, Q., Li, K.-D., Lian, J., and Wang, L., "Angular dependence of sputtering yield of amorphous and polycrystalline materials," *J. Phys. D Appl. Phys.*, Vol. 41, No. 17, 2008, p. 172002.

[30] Dankanich, J. W., Walker, M., Swiatek, M. W., and Yim, J. T., "Recommended Practice for Pressure Measurement and Calculation of Effective Pumping Speed in Electric Propulsion Testing," *J. Propul. Power*, Vol. 33, No. 3, 2017, pp. 668–680.